



# Structural characteristics and properties of heat-resistant nickel $\beta$ -alloys produced via the centrifugal SHS-casting method

V.V. Sanin<sup>1,2</sup>, M.I. Aheiev<sup>1</sup>, P.A. Loginov<sup>1</sup>, M.Ya. Bychkova<sup>1</sup>, E.S. Shukman<sup>2</sup>,  
L.Yu. Mezhevaia<sup>1,2</sup>, V.N. Sanin<sup>3</sup>, T.A. Lobova<sup>1</sup>

<sup>1</sup> National University of Science and Technology “MISIS”  
4 Bld. 1 Leninskiy Prosp., Moscow 119049, Russia

<sup>2</sup> JSC “Giredmet” n.a. N.P. Sazhin  
1 Bld. 2 Elektrodnyaya Str., Moscow 111524, Russia

<sup>3</sup> Merzhanov Institute of Structural Macrokinetics and Materials Science  
of the Russian Academy of Sciences  
8 Akademicheskaya Str., Chernogolovka, Moscow Region 142432, Russia

✉ Maksym I. Aheiev (aheievmi@gmail.com)

**Abstract:** Employing centrifugal self-propagating high-temperature synthesis (SHS) metallurgy, complemented by advanced metallurgical processes such as vacuum induction melting (VIM) and vacuum arc remelting (VAR), yielded the alloy formulation denoted as base–2.5Mo–1.5Re–1.5Ta–0.2Ti. This study investigates the effects of various technological modes and additional metallurgical treatments on the alloy's impurity and non-metallic inclusion content, structural characteristics, mechanical behavior under compression, and its oxidation mechanisms and kinetics when exposed to temperatures of 1150 °C for 30 h. With increasing centrifugal acceleration, the proportion of non-metallic inclusions (number of points) drops from 5 to 1–2 points. The best combination mechanical properties, including  $\sigma_{\text{UCS}} = 1640 \pm 20$  MPa,  $\sigma_{\text{ys}} = 1518 \pm 10$  MPa, and residual deformation were observed in alloys processed under conditions of increased gravitational force ( $g = 50$ ). Within a centrifugal force range of  $g = 20+300$ , the composition of the synthesis products aligned with the theoretical expectations. The total content of impurities is  $0.15 \pm 0.02$  %, with a decrease in gas impurities—oxygen and nitrogen levels reduced to 0.018 % and 0.0011 %, respectively. The structural analysis of the alloys revealed the presence of globular and streaked inclusions of a chromium-based solid solution embedded within the matrix. Inclusions with thickness of 2–8  $\mu\text{m}$  are present in the intergranular space:  $(\text{Cr})_{\text{Ni,Mo,Co}}$ ,  $(\text{Cr})_{\text{Mo,Re}}$  and  $(\text{Cr})_{\text{Re,Mo}}$ . The formation of the Ni(Al,Ti) phase at grain boundaries was identified, contributing to an enhancement in plastic resistance and overall strength of the alloy. Oxidation mechanisms varied across different processing modes, with the size of structural components significantly influencing oxidation kinetics. The weight gain observed in SHS samples was  $70 \pm 10$  g/m<sup>2</sup> with oxidation predominantly occurring along the NiAl interphase boundaries and penetrating into the depth of the sample. TEM facilitated the identification of phases enriched with Ti microadditions, reducing the levels of dissolved nitrogen and oxygen within the intermetallic phase to a combined weight percentage ( $\Sigma_{\text{O,N}}$ ) of 0.0223 wt.%.

**Keywords:** heat-resistant nickel alloys, centrifugal SHS-casting, centrifugal acceleration, SHS, vacuum induction melting (VIM), vacuum arc remelting (VAR), nonmetallic inclusions, gas impurity content, heat resistance, oxidation kinetics.

**Acknowledgments:** This research was supported by the Russian Science Foundation, grant No. 19-79-10226, <https://rscf.ru/project/19-79-10226/>

**For citation:** Sanin V.V., Aheiev M.I., Loginov P.A., Bychkova M.Ya., Shukman E.S., Mezhevaia L.Yu., Sanin V.N., Lobova T.A. Structural characteristics and properties of heat-resistant nickel  $\beta$ -alloys produced via the centrifugal SHS-casting method. *Izvestiya. Non-Ferrous Metallurgy*. 2024;30(1):24–41. <https://doi.org/10.17073/0021-3438-2024-1-24-41>

# Особенности структуры и свойства жаропрочных никелевых $\beta$ -сплавов, полученных методом центробежного СВС-литья

В.В. Санин<sup>1,2</sup>, М.И. Агеев<sup>1</sup>, П.А. Логинов<sup>1</sup>, М.Я. Бычкова<sup>1</sup>, Е.С. Шукман<sup>2</sup>,  
Л.Ю. Межевая<sup>1,2</sup>, В.Н. Санин<sup>3</sup>, Т.А. Лобова<sup>1</sup>

<sup>1</sup> Национальный исследовательский технологический университет «МИСИС»  
Россия, 119049, г. Москва, Ленинский пр-т, 4, стр. 1

<sup>2</sup> АО «Гиредмет» им. Н.П. Сажина  
Россия, 111524, г. Москва, ул. Электродная, 2, стр. 1

<sup>3</sup> Институт структурной макрокинетики и проблем материаловедения им. А.Г. Мерджанова РАН  
Россия, 142432, Московская обл., г. Черноголовка, ул. Академика Осипьяна, 8

✉ Максим Игоревич Агеев (aheievmi@gmail.com)

**Аннотация:** По технологии центробежной СВС-металлургии при разных технологических режимах и дополнительных металлургических переделах (вакуумный индукционный переплав и вакуумный дуговой переплав) получен сплав: base–2,5Mo–1,5Re–1,5Ta–0,2Ti. Исследовано влияние режимов на содержание неметаллических включений и примесей, особенности структуры, механические свойства при сжатии, кинетику и механизм окисления при температуре 1150 °С в течение 30 ч. С ростом центробежного ускорения доля неметаллических включений (балльность) снижается с 5 до 1–2 ед. Наилучшее сочетание свойств по соотношению прочности, предела текучести и остаточной деформации имеет сплав, полученный в условиях перегрузки  $g = 50$ :  $\sigma_b = 1640 \pm 20$  МПа,  $\sigma_{0,2} = 1518 \pm 10$  МПа. При значениях перегрузки  $g = 20+300$  состав продуктов синтеза соответствует расчетным значениям. Суммарное содержание примесей составляет  $0,15 \pm 0,02$  %, что находится в области допустимых значений. С увеличением центробежной силы уменьшается содержание газовых примесей: кислорода – до 0,018 %, азота – до 0,0011 %. Структура сплавов характеризуется образованием в матрице глобулярных и строчечных включений твердого раствора на основе Cr. В межзеренном пространстве присутствуют включения  $(Cr)_{Ni,Mo,Co}$ ,  $(Cr)_{Mo,Re}$  и  $(Cr)_{Re,Mo}$  толщиной 2–8 мкм. На границах зерен образуется фаза Ni(Al,Ti), обеспечивающая рост сопротивления пластической деформации и повышение прочности сплава. Механизм окисления сплавов, полученных по разным режимам, отличается. Существенное влияние на кинетику окисления оказывает размерный фактор структурных составляющих. Прирост массы СВС-образцов составляет  $70 \pm 10$  г/м<sup>2</sup>. Процесс окисления происходит по межфазным границам NiAl в глубь образца. С помощью просвечивающей электронной микроскопии идентифицированы фазы, содержащие микродобавки Ti, которые снижают содержание в интерметаллидной фазе растворенных азота и кислорода до значения  $\sum_{O,N} = 0,0223$  мас. %.

**Ключевые слова:** жаропрочные никелевые сплавы, центробежное СВС-литье, центробежное ускорение, вакуумный индукционный переплав (ВИП), вакуумный дуговой переплав (ВДП), неметаллические включения, содержание газовых примесей, жаростойкость, кинетика окисления.

**Благодарности:** Исследование выполнено за счет гранта Российского научного фонда № 19-79-10226, <https://rscf.ru/project/19-79-10226/>

**Для цитирования:** Санин В.В., Агеев М.И., Логинов П.А., Бычкова М.Я., Шукман Е.С., Межевая Л.Ю., Санин В.Н., Лобова Т.А. Особенности структуры и свойства жаропрочных никелевых  $\beta$ -сплавов, полученных методом центробежного СВС-литья. *Известия вузов. Цветная металлургия*. 2024;30(1):24–41.

<https://doi.org/10.17073/0021-3438-2024-1-24-41>

## Introduction

Heat-resistant intermetallic nickel alloys are extensively employed in the construction of engines. However, these alloys exhibit certain limitations, notably their relatively inferior mechanical strength and plasticity at ambient temperatures. Such properties not only hinder mechanical processing but also elevate the risk of material fracture [1–9]. To improve fracture toughness, the addition of various plasticizing additives, including Cr, Co, Mo, Ta, Re, Zr has been investigated [3–12]. Additionally, materials utilized in high-temperature sections of engines must meet stringent requirements regarding the oxidation resistance of their surfaces when exposed to elevated temperatures and to the effects of thermal cycling [3–6; 13–15].

Self-propagating high-temperature synthesis (SHS) and its variants, including elemental synthesis [8–10] and centrifugal SHS-casting [12; 16; 17], represent recognized methods for fabricating cast and powder materials based on  $\beta$ -alloys. Within this domain, efforts are concentrated on refining the compositional makeup and production methodologies of CompoNiAl alloys, particularly those derived from a NiAl–Cr–Co base, here and after referred to as ‘the base’ [12].

Research aimed at augmenting crack resistance at reduced temperatures has led to the exploration of microalloying techniques using diverse elements within these alloys. Studies have identified [11; 12; 16; 18; 19] that in cast SHS alloys formulated from the base + X (where X includes La, Mo, Ta, Re, Zr), the inclusion of Mo and Re is instrumental in promoting the development of a cellular eutectic structure. The introduction of 15 % Mo has been found to significantly bolster mechanical attributes, yielding  $\sigma_{\text{ucs}} = 1,604 \pm 80$  MPa,  $\sigma_{\text{ys}} = 1,520 \pm 80$  MPa, and  $\epsilon = 0.79$  %. Subsequent annealing at 1,250 °C for 180 min further enhances these properties increasing  $\sigma_{\text{ucs}}$  by 12 %,  $\sigma_{\text{ys}}$  by 10 %, and  $\epsilon$  by 100 %. The addition of 1.5 % rhenium to the base + 15Mo1.5Re alloy modifies its structural composition, thereby elevating mechanical properties to  $\sigma_{\text{ucs}} = 1,682 \pm 60$  MPa,  $\sigma_{\text{ys}} = 1,538 \pm 60$  MPa, and  $\epsilon = 0.87$  %, with further improvements observed following additional annealing:  $\sigma_{\text{ucs}}$  by 20 %,  $\sigma_{\text{ys}}$  by 7 %, and  $\epsilon$  by 640 %. A hierarchical three-level structure characterizes the base + 15%Mo alloy: the first level consists of  $\beta$ -NiAl dendritic grains interlaced with molybdenum-enriched phases  $(\text{Ni,Co,Cr})_3\text{Mo}_3\text{C}$  and  $(\text{Mo}_{0.8}\text{Cr}_{0.2})_x\text{B}_y$  with cell size up to 50  $\mu\text{m}$ ; the second level includes strengthening submicron Cr(Mo) particles along grain boundaries; and the third level encompasses coherent Cr(Mo) nanodeposits (10–40 nm) within  $\beta$ -NiAl dendrites. The

incorporation of alloying interstitial elements enhances the oxidation resistance of  $\beta$ -alloys by fostering the formation of additional phases [11]. The alloy that incorporates zirconium demonstrates superior heat resistance, with an oxidation rate of 21 g/m<sup>2</sup> over 30 h. The formation of a zirconium-rich continuous top layer comprising  $\text{Al}_2\text{O}_3 + \text{Zr}_3\text{Al}_3\text{O}_{0.5}$  obstructs external oxygen and nitrogen diffusion, thereby significantly improving heat resistance [18].

Currently, the alloy base–2.5Mo–1.5Re–1.5Ta–0.2Ti alloy represents the optimal composition, exhibiting strength characteristics with a tensile strength ( $\sigma_{\text{ucs}}$ ) of  $1644 \pm 30$  MPa, a yield strength ( $\sigma_{\text{ys}}$ ) of  $1518 \pm 25$  MPa, and a total weight gain during of oxidation 52 g/m<sup>2</sup> [19].

Maintaining a low concentration of impurities is crucial for the performance of heat-resistant alloys. The presence of residual metallic and gaseous elements, along with non-metallic inclusions, adversely affects the mechanical, technological, and thermal resistance characteristics of these alloys [20]. A technological approach to mitigate these effects involves the application of conventional metallurgical techniques to refine the alloy’s properties. Prior research on the base alloy [16] has demonstrated the beneficial influence of vacuum induction melting (VIM) and subsequent heat treatment (HT) processes on enhancing its properties. However, the application of VIM technology may introduce non-metallic inclusions into the alloy due to interactions between the metal and lining materials. Thus, it becomes essential to investigate the structural and property changes in alloys subjected to vacuum arc remelting (VAR) within a copper-cooled crystallizer.

This study aims to examine the influence of synthesis parameters (SHS-M) and additional treatment (VIM, VAR, HT) on the structural parameters, mechanical properties and resistance to high-temperature oxidation (heat resistance) of the base–2.5Mo–1.5Re–1.5Ta–0.2Ti alloy.

## Research materials and methods

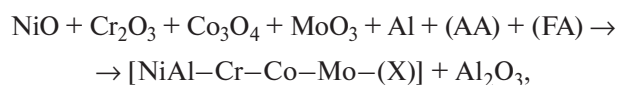
The synthesis was performed using a radial centrifugal apparatus, subject to high gravitational forces of up to 300 g. Reference [12] outlines the centrifugal apparatus’s overall configuration. The design of this apparatus allows for the precise adjustment of the centrifugal rotor’s speed, thus achieving the desired overload conditions. This technology is characterized by its use of readily available oxide raw materials and its capability to reach high combustion temperatures between 2100–3500 °C. Such temperatures facilitate the segre-

Table 1. Characteristics of initial components and modifying additions

Таблица 1. Характеристики исходных веществ и модифицирующих добавок

Substance	Brand	GOST/TS	Particle size, $\mu\text{m}$	Purity, %
Main components				
NiO	OSCh	TS 6-09-02439-87	<40	99.00
Cr <sub>2</sub> O <sub>3</sub>	Ch	TS 6-09-4272-84	<20	99.00
Co <sub>3</sub> O <sub>4</sub>	OSCh	GOST 18671-73	<30	99.00
Al	PA-4	GOST 6058-73	<140	98.00
Al	ASD-1	TS 48-5-226-87	<50	99.70
Modifying additions				
MoO <sub>3</sub>	ChDA	TS 6-09-4471-77	<50	99.00
Ta	TaPM	TS 48-19-72-92	<20	98.00
Re	Pe-0	TS 48-4-195-87	<150	99.99
Ti	PTOM-1	TS 14-22-57-92	$\leq 30$	99.80

gation of the target product phase from the slag phase. The chemical process involved can be summarized by the equation:



where AA (alloying addition) includes Mo, Re, Ta, and Ti; FA (functional addition) comprises CaF<sub>2</sub>, Na<sub>3</sub>[AlF<sub>6</sub>], etc.; X is a metal (Ta, Re, Ti).

Table 1 presents the classifications and characteristics of the initial powders used in the synthesis. Alloying additions were incorporated into the reaction mixture to achieve the specific desired composition of the alloy.

The preparing exothermic mixtures commenced with the drying of components within SNOL-type ovens ( $t = 90^\circ\text{C}$ ,  $\tau = 1\text{ h}$ ). Subsequent steps included the precise measurement of reagents, their mixing, and the placement of the resulting mixture into graphite molds. The mixing process utilized an MP4/0.5 planetary ball mill for a period of 15–20 min, with a jar capacity of 1 L and a ball-to-powder weight ratio set at 1 : 5. Due to the processing temperature of the mixtures surpassing the melting points of the end synthesis products, phase segregation was facilitated by the gravitational separation of the molten metal from the slag. Within the reaction mixture, tantalum (Ta), rhenium (Re), and ti-

tanium (Ti) were incorporated as pure elements, whereas molybdenum (Mo) was added in the form of MoO<sub>3</sub> oxide. The utilization of aluminum powder in varying grades served to regulate the self-propagating high-temperature synthesis (SHS) process [11; 12].

To evaluate the impact of impurity elements and non-metallic inclusions on the alloy's properties, additional processes were employed: vacuum induction melting (VIM) with subsequent ingot casting (slow crystallization;  $V_{\text{cooled } 1} = 50^\circ\text{C}/\text{min}$ ) and rod extrusion directly from the molten state (rapid crystallization,  $V_{\text{cooled } 2} = 250^\circ\text{C}/\text{min}$ ) for the base—2.5Mo—1.5Re—1.5Ta—0.2Ti alloy sample under an overload condition of  $g = 50$ , following by vacuum arc remelting (VAR) in the copper cooled crystallizer.

SHS ingots undergo melting within a vacuum induction melting furnace VIP-010. This furnace facilitates the melting of ingots within an corundum crucible, accommodating weights ranging from 0.5 to 10 kg, for subsequent pouring into a steel mold-crystallizer. The vacuum induction melting of the SHS ingot is executed within the vacuum arc remelting furnace, capable of producing ingots up to 500 g. An advantage of VAR lies in the absence of interaction between the liquid metal and the furnace lining materials at elevated temperatures, as the melting occurs within a cooled copper crystallizer. This process significantly diminishes the presence of non-metallic inclusions within the alloy.

Given the lack of standard regulatory documents for the metallographic assessment of intermetallic nickel-aluminum system alloys, we adopted the metallographic method designated for evaluating non-metallic inclusions in steel (GOST 1778-70). This approach was simplified by amalgamating all categories of non-metallic inclusions, aiming to demonstrate the feasibility of enhancing alloy quality through modifications in centrifugal acceleration values and supplementary furnace treatment. The comparative analysis of the produced ingots focused on qualitative improvements without delving into the precise quantitative presence of each non-metallic inclusion type. Sample sections for this evaluation were selected and prepared in strict adherence to GOST 1778-70 standards.

For the quantitative analysis of major elements and impurities, a suite of sophisticated analytical instruments was employed, including the Finnigan Element GD (glow discharge) mass spectrometer (Thermo Fisher Scientific, Germany), the iCAP 6300 inductively coupled plasma-atomic emission spectrometer (Thermo Fisher Scientific), and a Nier—Johnson double-focusing mass spectrometer. The analysis of carbon and sul-

fur content in metals was carried out using the SC844 analyzer (LECO, USA), while the determination of oxygen, nitrogen, and hydrogen concentrations utilized the ONH836 analyzer (LECO).

The phase composition of the materials was determined through  $X$ -ray diffraction phase analysis (XRD) employing a D2 PHASER diffractometer (Bruker AXS GmbH, Germany) with  $\text{CuK}\alpha$ -radiation within an angle range of  $2\theta = 10\div 140^\circ$ .

Microstructural analyses were conducted using the S-3400N scanning electron microscope (SEM) (Hitachi, Japan) equipped with the “NORAN System 7  $X$ -ray Microanalysis System” (Thermo Scientific, USA) for energy-dispersive spectrometry. Further investigation was facilitated by the JEM-2100 transmission electron microscope (TEM) (Jeol, Japan) with a double-tilt beryllium holder, utilizing lamellae prepared from pre-manufactured foil through the focused ion beam (FIB) method on the “Quanta 200 3D FIB” microscope (FEI Company, USA). The foils for TEM analysis were prepared via ion etching using the “PIPS II System” (Gatan, Inc., USA).

Mechanical compression testing at ambient temperature was executed on the LF-100KNa universal machine (Walter + Bai AG, Switzerland) according to GOST 25.503-97 standard.

Oxidative annealing experiments were performed in an open atmosphere at a temperature of  $1150^\circ\text{C}$  for 30 h, with sample weights measured periodically in the SShOL 1.1.6/12-M3 laboratory electric pit-type heating furnace. The mass change of samples over specified durations was calculated relative to the unit surface area. Oxidation curves and corresponding approximation equations were formulated based on the collected data. The parabolic oxidation rate constant ( $k_p$ ) for the studied alloys was calculated using the equation:

$$(\Delta m/S)^2 = k_p \tau, \quad (1)$$

where  $\Delta m$  is the change in mass,  $S$  is the surface area, and  $\tau$  is the time.

## Results and discussion

As the base—2.5Mo—1.5Re—1.5Ta—0.2Ti alloy was synthesized using the centrifugal installation, several key parameters were quantitatively assessed: the burning rate ( $U$ ) of the mixture, the scattering of the mixture ( $\eta_1$ ), and the completeness of the metal phase yield in the ingot ( $\eta_2$ ). The burning rate of the mixture during synthesis, under conditions of up to  $g = 20$  overload, was  $U = 13 \pm 1$  mm/s. An increase in overload to  $g = 300$  resulted in a heightened burning rate, recorded at  $U = 23 \pm 2$  mm/s. The parameter designated as the scattering of the mixture ( $\eta_1$ ) demonstrated a significant reduction only upon reaching the maximum overload value ( $g = 300$ ). Moreover, an incremental overload was associated with a uniform rise in the “yield ratio”, or the completeness of the metal phase yield ( $\eta_2$ ) (Table 2).

In this investigation, four ingots were synthesized under varying conditions (refer to the entries of 1–4 Table 2).

Additionally, to explore the impact of metallurgical processing on the alloy’s properties, three samples (5–7) received supplementary treatments:  $g = 50 + \text{VIM}$  into the ingot (5);  $g = 50 + \text{VIM}$  into the rod (6) and  $g = 50 + \text{VAR}$  (7).

Figure 1 presents a comparative analysis of the ratings assigned to the content of non-metallic inclusions, derived from the microstructural examination of the alloys utilizing an optical microscope.

The analysis of the alloy samples’ structures revealed several distinctive characteristics. The SHS alloy sample 1 ( $g = 1$ ) exhibited a dendritic structure accompanied by a considerable presence of heterogeneous inclusions and pores, a result of the absence of centrifugal acceleration during the alloy’s synthesis. This sample was assigned the maximum score (4–5 points) among the ones studied. SHS alloy sample 2 ( $g = 20$ ) displayed a structure predominantly composed of the metallic phase, albeit with inclusions averaging a score of 3 points.

Table 2. Synthesis parameters of the base—2.5Mo—1.5Re—1.5Ta—0.2Ti alloy

Таблица 2. Параметры синтеза сплава base—2,5Mo—1,5Re—1,5Ta—0,2Ti

Sample No.	Overload $g$	Burning rate $U$ , mm/s	Scattering of the mixture $\eta_1$ , %	Completeness of the metal phase yield in the ingot $\eta_2$ , %
1	1	12.8	4.2	79
2	20	13.3	3.8	84
3	50	22.6	3.8	92
4	300	25.8	1.8	98.7

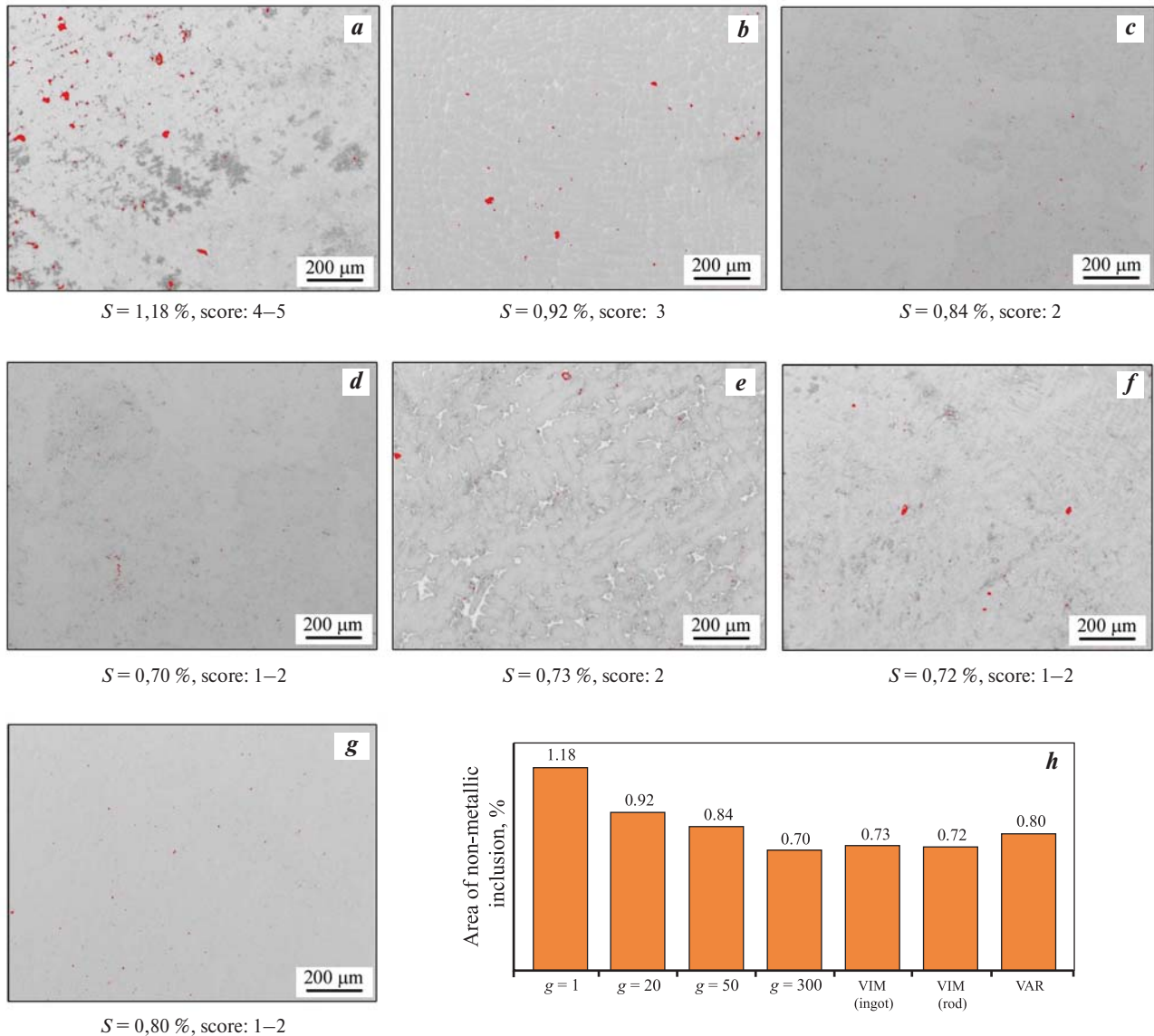


**Fig. 1.** Photographs and analysis of sections for non-metallic inclusion content in the base-2.5Mo-1.5Re-1.5Ta-0.2Ti alloy under various conditions and technologies

*a* – SHS,  $g = 1$ ; *b* – SHS,  $g = 20$ ; *c* – SHS,  $g = 50$ ; *d* – SHS,  $g = 300$ ; *e* – SHS ( $g = 50$ ) + VIM (ingot); *f* – SHS ( $g = 50$ ) + VIM (rod); *g* – SHS ( $g = 50$ ) + VAR; *h* – the content of non-metallic inclusion

**Рис. 1.** Фотографии и анализ шлифов на содержание неметаллических включений сплава base-2,5Mo-1,5Re-1,5Ta-0,2Ti при различных режимах и технологиях получения

*a* – CBC,  $g = 1$ ; *b* – CBC,  $g = 20$ ; *c* – CBC,  $g = 50$ ; *d* – CBC,  $g = 300$ ; *e* – CBC ( $g = 50$ ) + ВИП (в слиток); *f* – CBC ( $g = 50$ ) + ВИП (в стержень); *g* – CBC ( $g = 50$ ) + ВДП; *h* – содержание неметаллических включений

Exposure of the melt to an overload of  $g = 50$  resulted in the production of ingot 3, which exhibited a reduction in impurities and non-metallic inclusions, leading to an average score of 2 points. Further increases in overload did not significantly alter the inclusion rating, with sample 4 achieving an average score of 1–2 points. It is noteworthy that additional metallurgical processes (VIM, VAR) did not substantially decrease the inclusion scores (remaining within 1–2 points); however, these

treatments notably affected the sizes of the structural components.

A comprehensive examination of the alloys' microstructures through SEM is depicted in Fig. 2. This analysis revealed that at a centrifugal force of  $g = 20$ , the average size of the NiAl structural cells is  $90 \pm 10 \mu\text{m}$ , whereas at  $g = 300$ , the cell size significantly reduces to  $15 \pm 5 \mu\text{m}$ . The dimension of these structural constituents plays a crucial role in influencing the mechanical

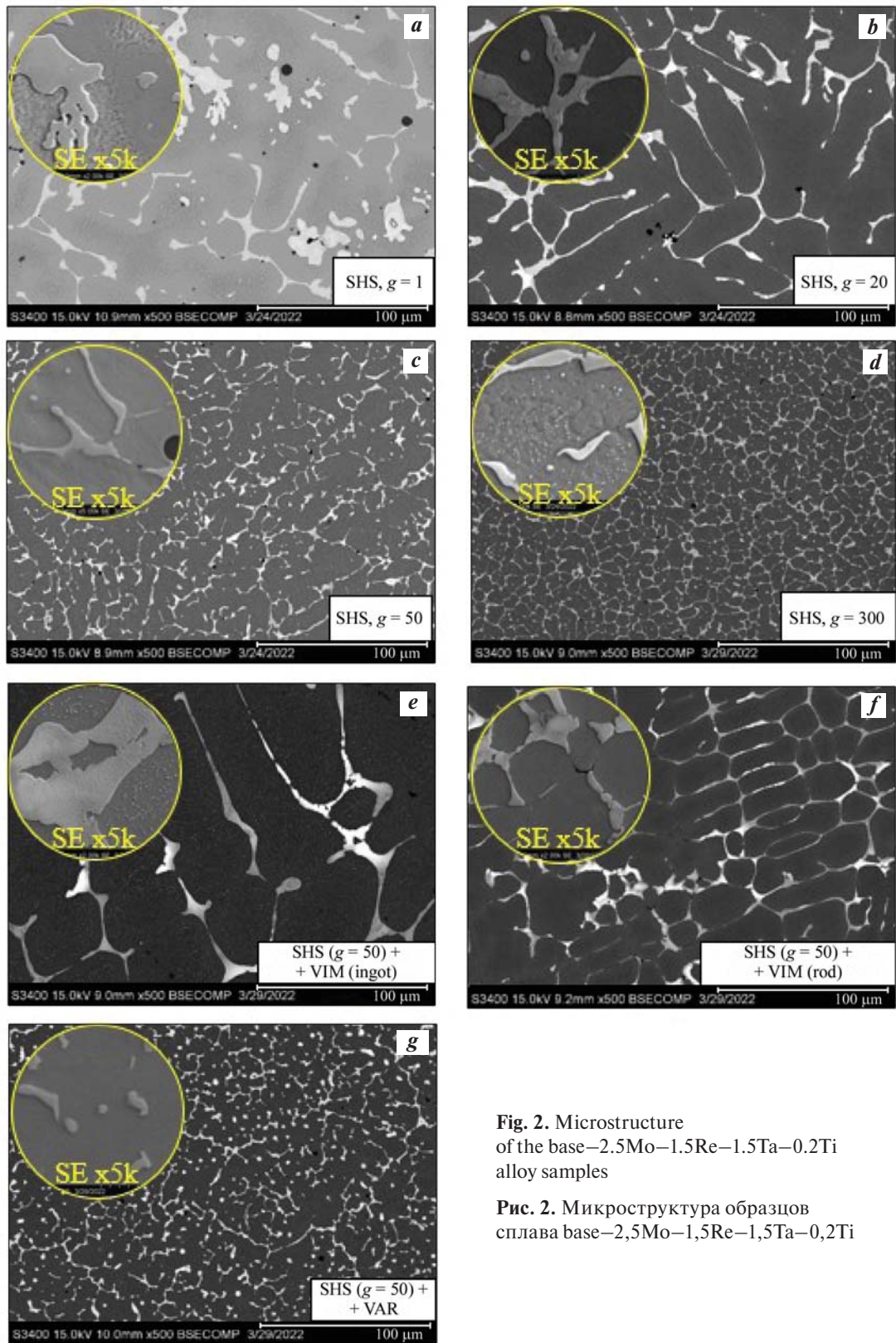


**Fig. 2.** Microstructure of the base-2.5Mo-1.5Re-1.5Ta-0.2Ti alloy samples

**Рис. 2.** Микроструктура образцов сплава base-2,5Mo-1,5Re-1,5Ta-0,2Ti

properties and oxidation resistance of the alloys [11; 20–22]. Studies [11; 19] emphasize the transformative effect of adding minute amounts of rhenium to the alloy's structure. At elevated overload values, the synthesized

molten products undergo intensive mixing, facilitating the uniform dispersion of refractory rhenium throughout the melt. Consequently, rhenium grains serve as crystallization nuclei during the cooling process. This phe-

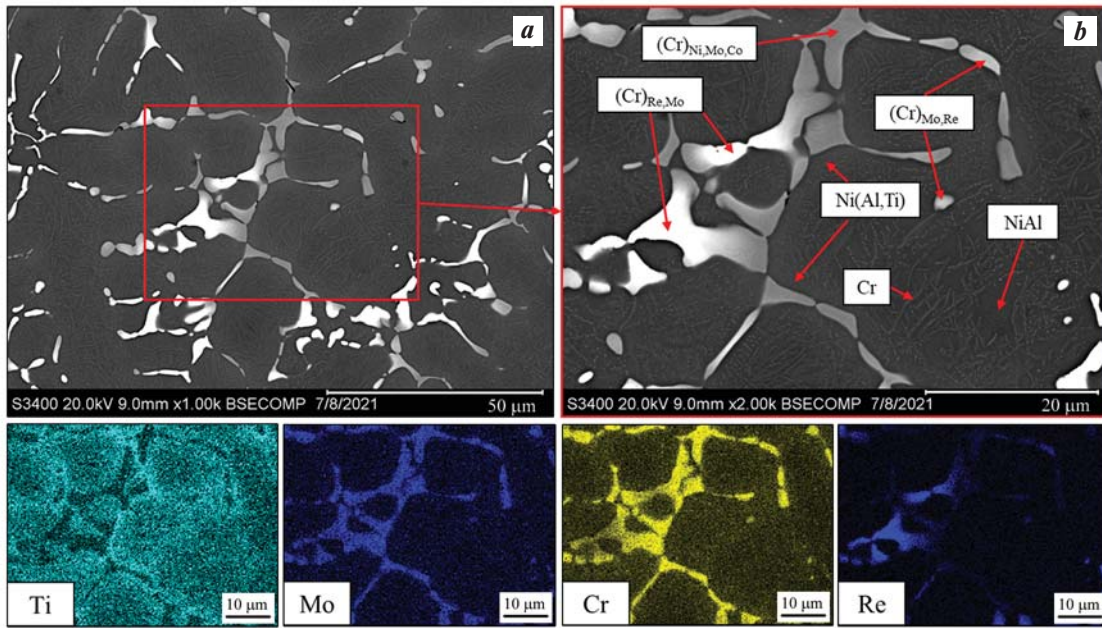


**Fig. 3.** Microstructure of the base–2.5Mo–1.5Re–1.5Ta–0.2Ti alloy ( $g = 50$ ) (a), focused area of analysis (b), and the distribution map of the main alloying elements

**Рис. 3.** Микроструктура сплава base–2,5Mo–1,5Re–1,5Ta–0,2Ti ( $g = 50$ ) (a), выделенная область анализа (b) и карта распределения основных легирующих элементов

**Table 3. Mechanical properties of the base–2.5Mo–1.5Re–1.5Ta–0.2Ti alloys**

Таблица 3. Механические свойства сплавов base–2,5Mo–1,5Re–1,5Ta–0,2Ti

Sample No.	Production technique	$\sigma_{ucs}$ , MPa	$\sigma_{ys}$ , MPa	$\epsilon$ , %
1	SHS, $g = 1$	730	–	$<1^*$
2	SHS, $g = 20$	813	–	$<1$
3	SHS, $g = 50$	1650	1522	1.95
4	SHS, $g = 300$	1634	1513	1.24
5	SHS ( $g = 50$ ) + VIM (ingot)	1304	1126	0.51
6	SHS ( $g = 50$ ) + VIM (rod)	1680	1555	1.34
	CBC ( $g = 50$ ) + VAR	1260	–	$<1$

\* The samples exhibited brittle fracture.

nomenon is corroborated by the chemical analysis of the alloy synthesized at  $g = 20$ , which indicates an increase in rhenium content corresponding with higher overload levels, from 1.37 % up to the anticipated concentration of  $1.5 \pm 0.2$ . Regarding the completeness of the metal phase yield in the ingot ( $\eta_2$  in Table 2), it is observed that in

the absence of centrifugal forces or at minimal overloads (below 20 g), rhenium partially transitions into the oxide (slag) phase. This transition is not economically viable, especially considering the high cost of rhenium.

Figure 3 shows the analysis of the structural components in alloy 3 ( $g = 50$ ). Within the  $\beta$ -NiAl matrix, the formation of globular and string-like micron and sub-micron inclusions of a chromium-based solid solution is noted. These inclusions, ranging from 2 to 8  $\mu\text{m}$  in thickness, are located within the intergranular spaces, comprising  $(\text{Cr})_{\text{Ni,Mo,Co}}$ ,  $(\text{Cr})_{\text{Mo,Re}}$  and  $(\text{Cr})_{\text{Re,Mo}}$ . The formation of the Ni(Al,Ti) phase at the grain boundaries is observed, contributing to an enhanced plastic resistance and overall strength of the alloy.

The mechanical properties of the base–2.5Mo–1.5Re–1.5Ta–0.2Ti alloy samples, synthesized under varying centrifugal accelerations (1–300 g) and subjected to additional metallurgical processes, are detailed in Table 3. Alloys produced under conditions of elevated centrifugal acceleration ( $g = 50\div 300$ ) exhibited optimal mechanical properties, with a tensile strength ( $\sigma_{ucs}$ ) of  $1640 \pm 20$  MPa and a yield strength ( $\sigma_{ys}$ ) of  $1518 \pm 10$  MPa. In contrast, samples subjected to vacuum induction melting (VIM) in ingot form showed deteriorated mechanical properties, with  $\sigma_{ucs}$  and  $\sigma_{ys}$  values of  $1304 \pm 10$  MPa and  $1126 \pm 10$  MPa, respectively. This reduction in mechanical strength is attributed

**Table 4. Content (wt.%) of alloying elements and impurities in base–2.5Mo–1.5Re–1.5Ta–0.2Ti alloys**

Таблица 4. Содержание (мас.%) легирующих элементов и примесей в сплавах base–2,5Mo–1,5Re–1,5Ta–0,2Ti

Element	Ordered composition	$g = 1$	$g = 20$	$g = 50$	$g = 300$	$g = 50 + \text{VIM}$ (ingot)	$g = 50 + \text{VIM}$ (rod)	$g = 50 + \text{VAR}$
Ti	0.15–0.25	0.13	0.15	0.21	0.20	0.17	0.19	0.12
Mo	2.0–3.0	1.83	2.11	2.46	2.48	2.44	2.46	2.56
Re	1.4–1.7	1.26	1.37	1.49	1.52	1.47	1.46	1.53
Ta	1.4–1.7	1.86	1.64	1.46	1.46	1.24	1.29	1.38
W	–	0.033	0.032	0.031	0.037	0.031	0.031	0.11
O	–	0.13	0.037	0.021	0.018	0.0016	0.0026	0.0018
N	–	0.0074	0.0068	0.0013	0.0011	0.0001	0.0001	0.0001
C	–	0.013	0.014	0.017	0.017	0.011	0.011	0.011
S	–	0.0046	0.0041	0.0033	0.0032	<0.0005	<0.0005	<0.0005
$\Sigma_1$	–	0.1627	0.1533	0.1716	0.1543	0.1498	0.1502	0.2236
$\Sigma_2$	–	0.1410	0.1374	0.0223	0.0191	0.0017	0.0027	0.0019

Примечание.  $\Sigma_1$  – impurity content;  $\Sigma_2$  – sum of gas impurities.

to the growth in grain size resulting from slow cooling rates ( $V_{\text{cooled } 1} = 50 \text{ }^\circ\text{C}/\text{min}$ ). An indirect confirmation of the influence of cooling rates on mechanical properties is observed in the SHS + VIM (rod) samples. Unlike the ingot samples, these 8-mm diameter rods were extruded from the melt under identical processing conditions but cooled at a rate akin to that of the SHS process ( $V_{\text{cooled } 2} = 250 \text{ }^\circ\text{C}/\text{min}$ ), resulting in superior mechanical properties:  $\sigma_{\text{ucs}} = 1680 \pm 10 \text{ MPa}$  and  $\sigma_{\text{ys}} = 1555 \pm 10 \text{ MPa}$ . This suggests that by leveraging additional thermal post-treatment, it is possible to enhance the mechanical properties of the alloy, as corroborated by previous research [11; 12; 16].

Managing the chemical composition of alloys and minimizing the presence of undesirable impurities is a crucial aspect of the alloy synthesis process. Table 4 outlines the concentrations of principal alloying elements and impurities in the synthesized multicomponent base–2.5Mo–1.5Re–1.5Ta–0.2Ti alloys under various overload conditions and subsequent metallurgical treatments.

Chemical analyses of samples processed through differing technological protocols indicated alignment with the anticipated compositions at overloads  $g = 20\div 300$ . The chemical composition showcased optimal characteristics at overloads between  $g = 50$  and 300. Impurities such as Mg, Na, Si, Ca, K, Mn, and Cu are incidental,

originating from the initial reagents and incorporated into the synthesis products. The aggregate impurity content remained within an acceptable limit of  $0.15 \pm 0.02 \%$ . The tungsten (W) content increased across all samples to a maximum of 0.04 %, likely introduced from the grinding balls during material mixing. After VAR, tungsten concentration further escalated to 0.11 wt.%, attributable to process-specific dynamics and interactions between the melt and the material of the non-consumable electrode (W).

Regarding gas impurities (O, N) – critical for alloy workability – a decreasing trend in their concentrations was observed with increasing centrifugal force. Oxygen content diminished from 0.13 % at  $g = 1$  to 0.018 % at  $g = 300$ , while nitrogen content decreased from 0.0074 to 0.0011 %. These gas impurities influence not only mechanical properties but also the oxidation mechanism. VIM and VAR significantly alter the impurity profile; post-VIM processing reduced oxygen content in the ingot from 0.018 to 0.0016 % and nitrogen content from 0.0011 to 0.0001 %. However, this also affected the ratios of fusible elements (Cr, Ta, Al, Ti), thereby impacting the alloy’s composition and properties.

The subsequent phase of the study focused on evaluating the effects of impurities and non-metallic inclusions on the properties of the base–2.5Mo–1.5Re–1.5Ta–

**Table 5. Impact of alloying additions on the oxidation kinetics of base–2.5Mo–1.5Re–1.5Ta–0.2Ti cast alloys**  
 Таблица 5. Влияние легирующих добавок на кинетику окисления литых сплавов base–2,5Mo–1,5Re–1,5Ta–0,2Ti

Sample No.	Production technique	Approximation equation	Weight gain, g/m <sup>2</sup>
2	SHS, g = 20	$y = 0.0021x^2 + 2.1508x + 4.091$	70.5
3	SHS, g = 50	$y = -0.0006x^3 + 0.0038x^2 + 3.0137x + 1.5265$	78.8
4	SHS, g = 300	$y = -0.0315x^2 + 2.9026x + 3.3651$	62.7
5	SHS (g = 50) + VIM (ingot)	$y = -0.0022x^4 + 0.1539x^3 - 3.7188x^2 + 45.51x + 22.95$	421.5
6	SHS (g = 50) + VIM (rod)	$y = -0.0009x^3 + 0.0466x^2 + 0.8678x + 1.6188$	45.1
7	SHS (g = 50) + VAR	$y = 8.6204x^{0,9}$	183.58

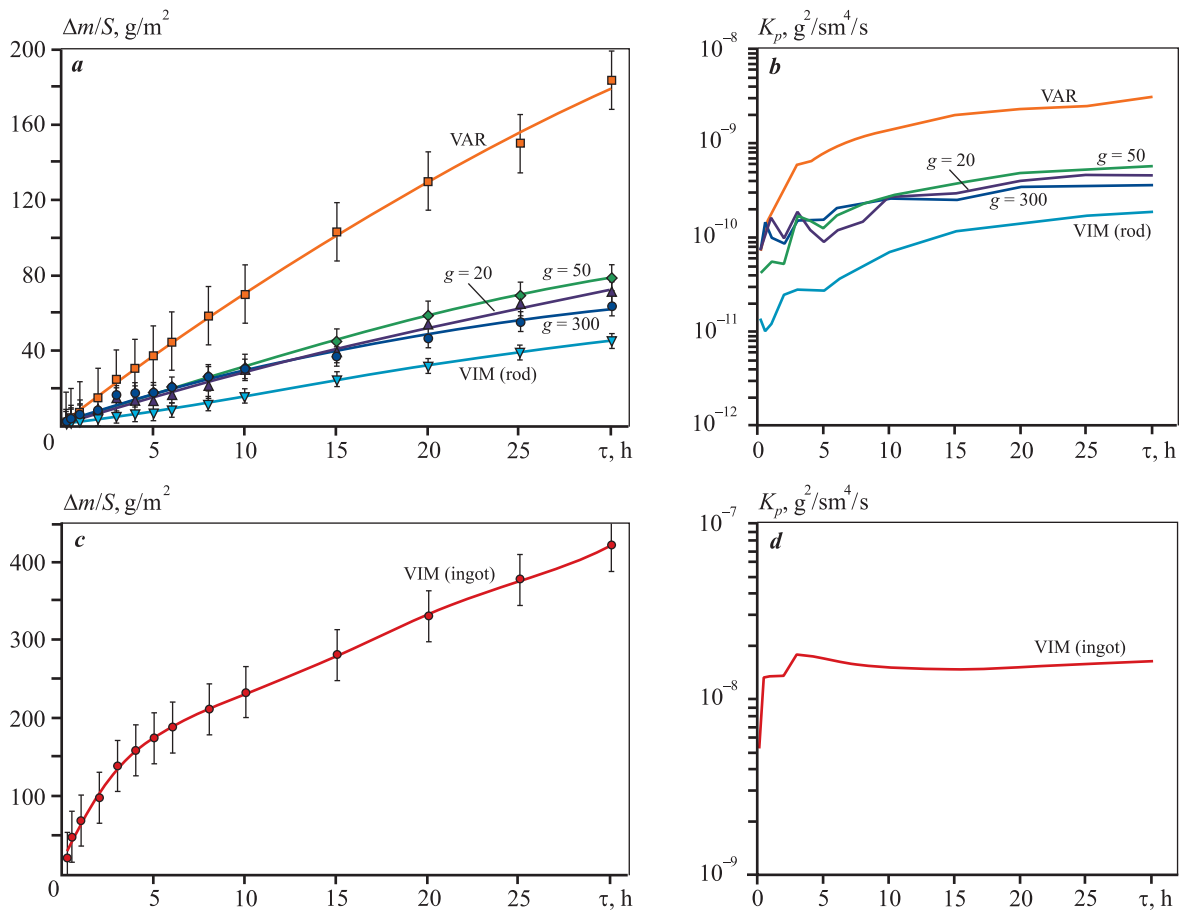


**Fig. 4.** Oxidation kinetic curves (a, b) and rate constant ( $k_p$ ) (b, d) for base–2.5Mo–1.5Re–1.5Ta–0.2%Ti alloys at 1150 °C for 30 h

**Рис. 4.** Кинетические кривые (a, б) и константа скорости ( $k_p$ ) окисления (б, д) сплавов base–2,5Mo–1,5Re–1,5Ta–0,2%Ti при температуре 1150 °C в течение 30 ч

0.2Ti alloy through oxidative annealing conducted in an open environment at 1150 °C for 30 h, with periodic sample weighing.

The ingot synthesized at  $g = 1$  was omitted from the experimental series due to non-compliance with chemical composition standards and inadequate mechanical

performance. Table 5 details the mass gains of samples following oxidative annealing and the derived approximation equations corresponding to the oxidation curves depicted in Fig. 4. Additionally, Fig. 4 illustrates the parabolic oxidation rate constant curves for the examined alloys.

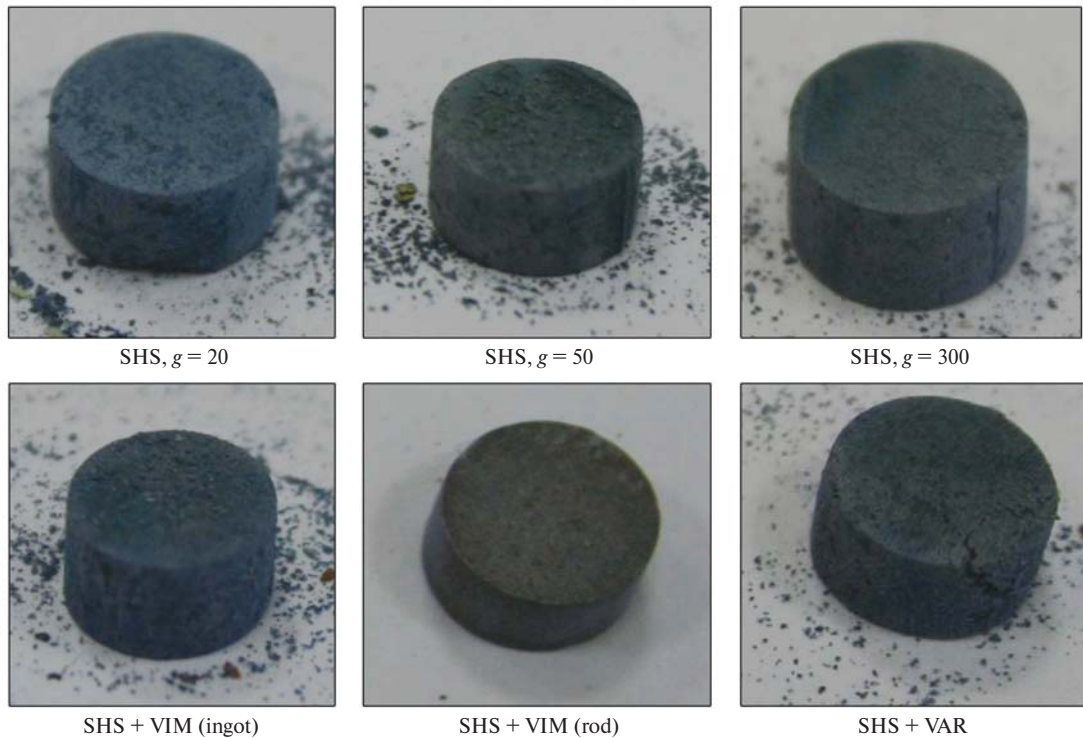


**Fig. 5.** Appearance of base–2.5Mo–1.5Re–1.5Ta–0.2Ti alloy samples after annealing at a 1150 °C for 30 h

**Рис. 5.** Внешний вид образцов сплавов base–2,5Mo–1,5Re–1,5Ta–0,2Ti после отжига при температуре 1150 °C в течение 30 ч

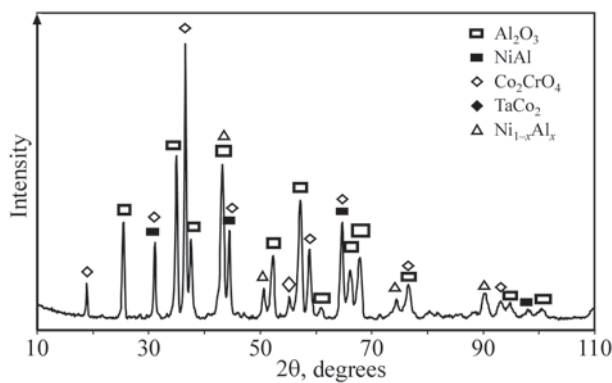


**Fig. 6.** Diffraction spectra of oxidized surface of the base–2.5Mo–1.5Re–1.5Ta–0.2Ti alloy

**Рис. 6.** Дифракционные спектры окисленной поверхности сплава base–2,5Mo–1,5Re–1,5Ta–0,2Ti

For all samples, except for the one subjected to VAR, the oxidation behavior aligns with the parabolic law, indicative of a typical oxidation process. Initially, during oxidation, a dense protective oxide layer forms across the surface of all alloys, significantly inhibiting further oxidation. The oxidation pattern for the VAR-treated sample adheres to an exponential law, demonstrating an atypical oxidation course. This anomaly is evidenced

by the initial destruction of the oxide layer, followed by the development of a crack within the sample itself (at  $\tau = 11\div 12$  h), a phenomenon substantiated by photographic documentation post 30 h of oxidative annealing (Fig. 5).

The diffraction spectra of the surfaces of  $\beta$ -alloys, oxidized at a  $t = 1150$  °C ( $\tau = 30$  h), are depicted in Fig. 6. Predominant peaks correspond to the phases of  $\gamma$ - $\text{Al}_2\text{O}_3$  aluminum oxide and  $\text{Co}_2\text{CrO}_4$  spinel, constituting the primary oxidation products and forming the protective upper layer. Alongside these oxides, phases based on nickel aluminide are detected, with alloying additions transitioning into a solid solution.

The oxidation mechanism across all samples under investigation is uniform, where oxygen and nitrogen infiltrate the alloy through the destructible  $\text{Al}_2\text{O}_3$  oxide surface film and a porous layer of  $\text{Co}_2\text{CrO}_4$  spinel. The presence of non-metallic inclusions or impurities within the alloy exhibits negligible influence on the high-temperature oxidation process. As indicated by the oxidation kinetic curves (refer to Fig. 4) and microstructural images of the oxidized layer (Fig. 7), all SHS samples ( $g = 20\div 300$ ) similar oxidation dynamics, featuring the formation of top oxide and nitride layers adjacent to the alloy. The observed weight gain is  $70 \pm 10$  g/m<sup>2</sup>. The

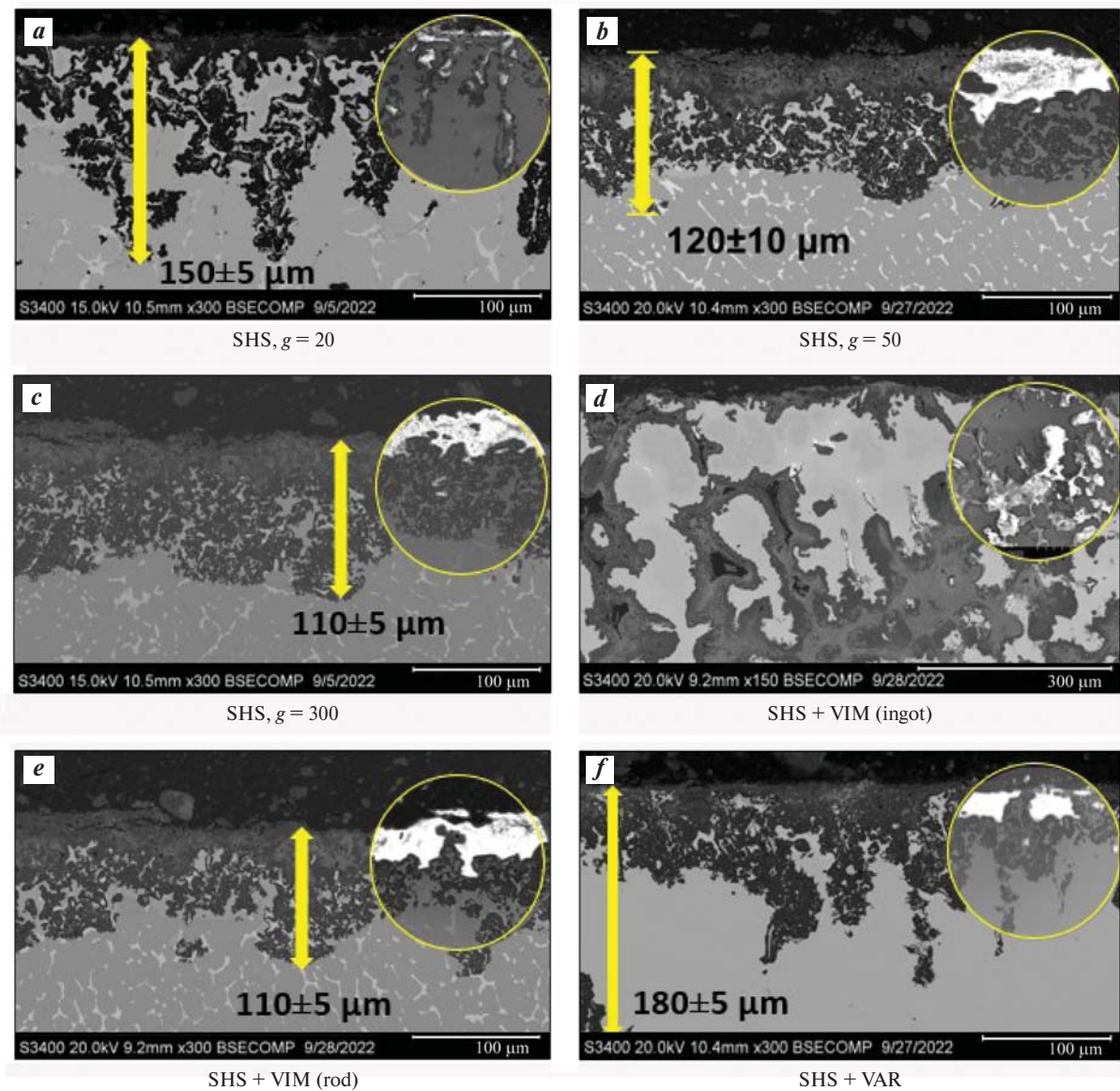


**Fig. 7.** Microstructure of base-2.5Mo-1.5Re-1.5Ta-0.2Ti alloy samples after annealing at 1150 °C for 30 h

**Рис. 7.** Микроструктура образцов сплавов base-2,5Mo-1,5Re-1,5Ta-0,2Ti после отжига при температуре 1150 °C в течение 30 ч

SHS sample synthesized at  $g = 20$  is distinguished by the wedge-like penetration of aluminum nitrides into the ingot along the grain boundaries, which contributes to an increased oxide layer thickness. The mass gain for the SHS + VIM (rod) sample registers at  $45.1 \pm 10 \text{ g/m}^2$ , likely attributable to the diminution of deleterious gas impurities from  $\Sigma_{\text{O,N}} = 0.0191 \text{ wt.}\%$  in the SHS sample ( $g = 300$ ) to  $\Sigma_{\text{O,N}} = 0.0027$  in the SHS + VIM (rod) sample. The dissolved nitrogen and oxygen content markedly affects both the kinetics and mechanism of oxidation. [18; 19]. However, the impact of dissolved gases on oxidation mechanisms must be evaluated in conjunction with the scale of structural constituents.

The VIM ingot sample, cooled at a different rate and characterized by larger dendritic sizes, displayed distinct oxidation kinetics and mechanism. This sample witnessed an oxidized layer thickness exceeding 250  $\mu\text{m}$ , with oxidation progressing along  $\beta$ -phase interphase boundaries. Its substantial mass gain during oxidation ( $\tau = 30 \text{ h}$ ;  $421 \pm 5 \text{ g/m}^2$ ) is attributed to intense oxidation ( $k_p = 5.28 \cdot 10^{-9} + 1.64 \cdot 10^{-8} \text{ g}^2/\text{cm}^4/\text{s}$ ), where Cr and Mo form volatile oxides that sublime without forming additional protective layers, leaving no continuous aluminum oxide layer on the sample's surface.

The SHS + VAR sample also recorded a high mass gain during oxidation ( $\tau = 30 \text{ h}$ ;  $183 \pm 5 \text{ g/m}^2$ ), with no-

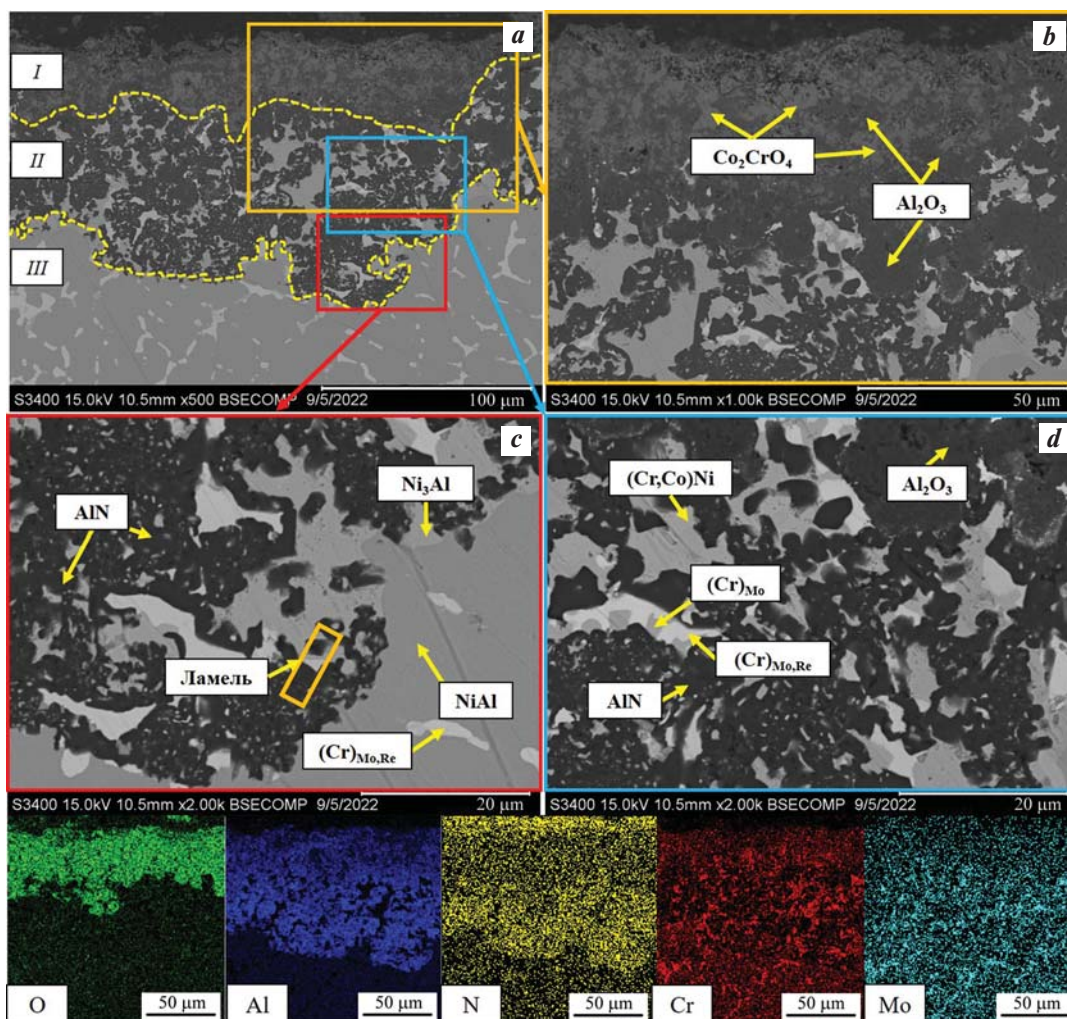
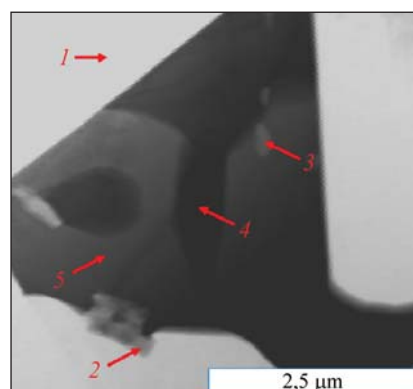


**Fig. 8.** Surface microstructure of oxidized (a) base–2.5Mo–1.5Re–1.5Ta–0.2Ti sample ( $g = 50$ ), selected areas for analysis (b–d), element distribution maps, lamellae cutting site (c)

**Рис. 8.** Микроструктура поверхности окисленного образца (a) состава base–2,5Mo–1,5Re–1,5Ta–0,2Ti ( $g = 50$ ), выделенные области анализа (b–d), карты распределения элементов и место резки ламели (c)

table crack formation after 12 h (Fig. 5) shows a crack formed after 12 h of oxidation. Analysis (Fig. 5 and 7) reveals that structural components’ dimensional factors resemble those in other samples, but the oxidation kinetics change with alterations in chemical composition due to the VAR process. This process increases the tungsten content to 0.11 wt.%, while reducing the presence of tantalum and other elements (refer to Table 4).

The examination of the oxidized surface of sample 3 of the base–2.5Mo–1.5Re–1.5Ta–0.2Ti alloy ( $g = 50$ ) is depicted in Fig. 8. This alloy is composed of three distinct layers. The uppermost oxide layer, measuring 40 μm in thickness and comprising Al<sub>2</sub>O<sub>3</sub> and Co<sub>2</sub>CrO<sub>4</sub> spinel, is notable for its low density and the presence of numerous pores. Beneath this layer lies a thin, continuous sublayer of Al<sub>2</sub>O<sub>3</sub> (5–10 μm thick) that acts as a barrier against oxygen infiltration into the ma-

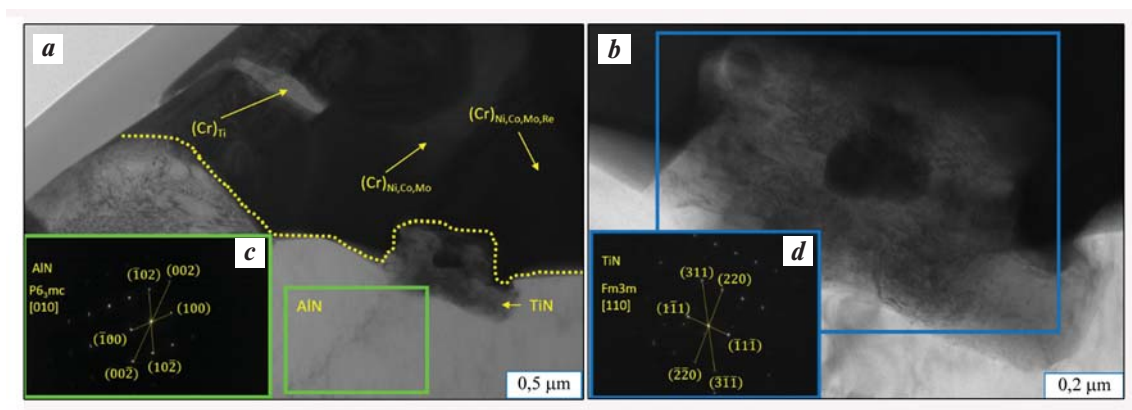


**Fig. 9.** TEM image and EDS analysis areas of lamella from oxidized layer of base–2.5Mo–1.5Re–1.5Ta–0.2Ti sample ( $g = 50$ ) in the Me–MeO transition layer

**Рис. 9.** ПЭМ изображение ламели из окисленного слоя образца base–2,5Mo–1,5Re–1,5Ta–0,2Ti ( $g = 50$ ) и области ЭДС в переходном слое Me–MeO

Table 6. Chemical composition (at.%) of lamella from oxidized layer of base–2.5%Mo–1.5%Re–1.5%Ta–0.2%Ti sample ( $g = 50$ )Таблица 6. Химический состав (ат.%) ламели из окисленного слоя образца base–2,5Mo–1,5Re–1,5Ta–0,2Ti ( $g = 50$ )

Spectrum	N	Al	Ti	Cr	Co	Ni	Mo	Re
1	38.71	61.29	–	–	–	–	–	–
2	52.83	–	40.24	5.63	0.38	0.93	–	–
3	–	–	21.79	48.61	5.76	18.35	5.49	–
4	–	–	–	49.31	12.33	20.40	10.83	7.13
5	7.28	–	–	54.11	7.36	24.04	7.20	0.00

Fig. 10. TEM image of transition layer in base–2.5Mo–1.5Re–1.5Ta–0.2Ti sample ( $g = 50$ )

*a* – distribution of structural components; *b* – enlarged view of TiN phase; *c* – X-ray diffraction pattern from AlN grain along zone axis [010]; *d* – X-ray diffraction pattern from TiN grain along zone axis [110]

Рис. 10. ПЭМ-изображение структурных составляющих переходного слоя образца base–2,5Mo–1,5Re–1,5Ta–0,2Ti ( $g = 50$ )

*a* – распределение структурных составляющих в ламели; *b* – увеличенная область фазы TiN; *c* – электронограмма с зерна AlN вдоль оси зоны [010]; *d* – электронограмма с зерна TiN вдоль оси зоны [110]

terial. Adjacent to the substrate, a substantial layer (up to 100  $\mu\text{m}$  thick) predominated by AlN features inclusions of chromium-containing phases such as (Cr,Co)Ni, (Cr)<sub>MoRe</sub>, and (Cr)<sub>Mo</sub>.

TEM studies were conducted to detail the composition of dispersed phases located along the AlN grain boundaries in the intermediate layer near the substrate. A lamella was extracted from the cross-section of the metal-nitride (MeN–Me) transition layer, with its position depicted in Fig. 8, *c*. The structure of this lamella is illustrated in Figs. 9 and 10, with specific analysis sites marked in Fig. 9. These sites were identified using the EDS method (spectra 1–5), and the findings are documented in Table 6. AlN, exhibiting a hexagonal crystal structure (space group  $P6_3mc$ ) with lattice parameters  $a = 3.078 \text{ \AA}$  and  $c = 5.004 \text{ \AA}$ , is identified as the principal phase of the transition layer (Fig. 9, Table 6, spect-

rum 1). Nitrogen diffusing along the grain boundaries of the porous oxide layer  $\text{Al}_2\text{O}_3 + \text{Co}_2\text{CrO}_4$  into the alloy's depth, and nitrogen impurities in the alloy, react with the aluminum in the matrix to form AlN. This interaction leads to a localized depletion of aluminum in the alloy, resulting in the creation of chromium (Cr)-based solid solutions with a BCC crystal lattice (space group  $\text{Im}3m$ ), containing Ti, Co, Ni, Mo, and Re in concentrations ranging from 5 to 24 at.% (Fig. 9, Table 6, spectra 3–5). Moreover, the oxidized layer contains submicron grains of a titanium-containing phase, likely TiN nitride (spectrum 2).

At the interface of the solid solution of chromium (Cr) and AlN aluminum nitride, submicron inclusions of the HCC-phase of TiN with a lattice parameter  $a = 4.207 \text{ \AA}$  were observed (Fig. 10). The formation of TiN, in reducing the alloy's dissolved nitrogen content

(refer to Table 4), also activates the diffusion of aluminum towards the surface. This process facilitates the formation of a dense oxide layer, thereby enhancing the alloy's heat resistance.

Investigating the effects of impurities and non-metallic inclusions on the mechanical properties and oxidation kinetics of the base—2.5Mo—1.5Re—1.5Ta—0.2Ti alloy is crucial for devising the optimal ingot production method to achieve superior alloy characteristics.

## Conclusions

1. The investigation elucidated the significant impact of centrifugal acceleration and subsequent metallurgical treatments (VIM) and VAR) on the structural, mechanical, and thermal resistance characteristics of the base—2.5Mo—1.5Re—1.5Ta—0.2Ti alloy.

2. Evaluation of the samples, adhering to GOST 1778-70 and amalgamating all categories of non-metallic inclusions, demonstrated a reduction in the presence of non-metallic inclusions from 5 to 1–2 points with an increase in centrifugal acceleration. The optimal centrifugal acceleration was identified as  $g = 50$ , beyond which the reduction in inclusion count was not significantly observed. While metallurgical processing (VIM, VAR) did not notably affect the inclusion score, it resulted in the noticeable growth of grain size.

3. Within the  $\beta$ -phase matrix, the presence of globular micron and submicron inclusions of a chromium solid solution was noted. Inclusions  $(Cr)_{Ni,Mo,Co}$ ,  $(Cr)_{Mo,Re}$  and  $(Cr)_{Re,Mo}$  with a thickness of 2–8  $\mu m$  are formed in the intergrain space. Additionally, the formation of the Ni(Al,Ti) phase at grain boundaries was observed, contributing to an enhanced resistance to plastic deformation and increased alloy strength.

4. The best combination mechanical properties, including tensile strength ( $\sigma_{ucs}$ ), yield strength ( $\sigma_{ys}$ ), and residual deformation, were observed in alloys synthesized under overload conditions of  $g = 50$  to 300, achieving  $\sigma_{ucs} = 1640 \pm 20$  MPa and  $\sigma_{ys} = 1518 \pm 10$  MPa. The SHS + VIM samples (ingot) exhibited deteriorated mechanical properties ( $\sigma_{ucs} = 1304 \pm 10$  MPa and  $\sigma_{ys} = 1126 \pm 10$  MPa), attributed to the enlargement of structural components due to slow cooling rates ( $V_{cooled\ 1} = 50$  °C/min).

5. Impurity elements such as Mg, Na, Si, Ca, K, Mn, Cu were identified as incidental, originating from the initial reagents. The total impurity content remained within acceptable limits of  $0.15 \pm 0.02$  %. Notably, an increase in centrifugal acceleration resulted in a decrease in the levels of impurity oxygen and nitrogen.

## References

1. Ying Wang, Hong-bo Guo, Hui Peng, Li-quan Peng, Sheng-kai Gong. Diffusion barrier behaviors of (Ru,Ni) Al/NiAl coatings on Ni-based superalloy substrate. *Intermetallics*. 2011;19(2):191–195. <https://doi.org/10.1016/j.intermet.2010.08.016>
2. Dongjun Wang, Ying Liang, Hanwei Ning, Bao Wang. Effects of Zr and Co on the microstructure and mechanical properties of NiAl-based alloys. *Journal of Alloys and Compounds*. 2021;883:160815. <https://doi.org/10.1016/j.jallcom.2021.160815>
3. Sui X., Lu J., Wei D., Zhang L., Wang R., Zhao W., Zhang W. Unveiling the influence of TiN on the microstructure and high-temperature oxidation behavior of Ti—Al—Cr composite coating. *Corrosion Science*. 2022;206:110539. <https://doi.org/10.1016/j.corsci.2022.110539>
4. Shang Z., Shen J., Wang L., Du Y., Xiong Y., Fu H. Investigations on the microstructure and room temperature fracture toughness of directionally solidified NiAl—Cr(Mo) eutectic alloy. *Intermetallics*. 2015;57:25–33. <https://doi.org/10.1016/j.intermet.2014.09.012>
5. Hu L., Zhang G., Hu W., Gottstein G., Bogner S., Bührig-Polaczek A. Tensile creep of directionally solidified NiAl—9Mo in situ composites. *Acta Materialia*. 2013;61(19):7155–7165. <https://doi.org/10.1016/j.actamat.2013.08.017>
6. Grabke H.J. Oxidation of NiAl and FeAl. *Intermetallics*. 1999;7(10):1153–1158. [https://doi.org/10.1016/S0966-9795\(99\)00037-0](https://doi.org/10.1016/S0966-9795(99)00037-0)
7. Kovalev A., Wainstein D., Rashkovskiy A. Influence of Al grain boundaries segregations and La-doping on embrittlement of intermetallic NiAl. *Applied Surface Science*. 2015;354:323–327. <https://doi.org/10.1016/j.apsusc.2015.06.110>
8. Kaplanskii Yu.Yu., Levashov E.A., Korotitskiy A.V., Loginov P.A., Sentyurina Zh.A., Mazalov A.B. Influence of aging and HIP treatment on the structure and properties of NiAl-based turbine blades manufactured by laser powder bed fusion. *Additive Manufacturing*. 2020;31:100999. <https://doi.org/10.1016/j.addma.2019.100999>
9. Levashov E.A., Mukasyan A.S., Rogachev A.S., Shtansky D.V. Self-propagating high-temperature synthesis of advanced materials and coatings. *International Materials Reviews*. 2017; 62(4): 203–239. <https://doi.org/10.1080/09506608.2016.1243291>
10. Kurbatkina V.V. Nickel aluminides. In: *Concise encyclopedia of self-propagating high-temperature synthesis*. Elsevier, 2017. P. 212–213. <https://doi.org/10.1016/B978-0-12-804173-4.00099-5>
11. Sanin V.V., Kaplansky Y.Y., Aheiev M.I., Levashov E.A.,

- Petrzhik M.I., Bychkova M.Ya., Samokhin A.V., Fadeev A.A., Sanin V.N. Structure and properties of heat-resistant alloys NiAl–Cr–Co–X (X = La, Mo, Zr, Ta, Re) and fabrication of powders for additive manufacturing. *Materials*. 2021;14(12):3144. <https://doi.org/10.3390/ma14123144>
12. Zaitsev A.A., Sentyurina Zh.A., Levashov E.A., Pogozhev Yu.S., Sanin V.N., Loginov P.A., Petrzhik M.I. Structure and properties of NiAl–Cr(Co,Hf) alloys prepared by centrifugal SHS casting. Part 1 – Room temperature investigations. *Materials Science and Engineering: A*. 2017;690:463–472. <https://doi.org/10.1016/j.msea.2016.09.075>
  13. Klumpes R., Maree C.H.M., Schramm E., de Wit J.H.W. The influence of chromium on the oxidation of  $\beta$ -NiAl at 1000 °C. *Materials and Corrosion*. 1996;47(11):619–624. <https://doi.org/10.1002/mac0.19960471105>
  14. Bo Li, Fei Liu, Cong Li, Yimin Gao, Congmin Fon, Xiaohu Hou. Effect of Cr element on the microstructure and oxidation resistance of novel NiAl-based high temperature lubricating composites. *Corrosion Science*. 2021;188:109554. <https://doi.org/10.1016/j.corsci.2021.109554>
  15. Gao W., Li Z., Wu Z., Li S., He Y. Oxidation behavior of Ni<sub>3</sub>Al and FeAl intermetallics under low oxygen partial pressures. *Intermetallics*. 2002;10(3):263–270. [https://doi.org/10.1016/S0966-9795\(01\)00132-7](https://doi.org/10.1016/S0966-9795(01)00132-7)
  16. Zaitsev A.A., Sentyurina Zh.A., Levashov E.A., Pogozhev Yu.S., Sanin V.N., Sidorenko D.A. Structure and properties of NiAl–Cr(Co,Hf) alloys prepared by centrifugal SHS casting followed by vacuum induction remelting. Part 2 – Evolution of the structure and mechanical behavior at high temperature. *Materials Science and Engineering: A*. 2017;690:473–481. <http://doi.org/10.1016/j.msea.2017.02.089>
  17. Kaplanskii Yu.Yu., Zaitsev A.A., Levashov E.A., Pogozhev Yu.S., Loginov P.A., Sentyurina Zh.A., Logacheva A.I. The structure and properties of pre-alloyed NiAl–Cr(Co,Hf) spherical powders produced by plasma rotating electrode processing for additive manufacturing. *Journal of Materials Research and Technology*. 2018;7(4):461–468. <https://doi.org/10.1016/j.jmrt.2018.01.003>
  18. Aheiev M.I., Sanin V.V., Shvindina N.V., Kaplanskii Yu.Yu., Levashov E.A. Oxidation kinetics and mechanism of nickel alloys. *Powder Metallurgy and Functional Coatings*. 2022;(3):4–23. <https://doi.org/10.17073/1997-308X-2022-3-4-23>  
Агеев М.И., Санин В.В., Швындина Н.В., Капланский Ю.Ю., Левашов Е.А. Кинетика и механизм окисления никелевых сплавов. *Известия вузов. Порошковая металлургия и функциональные покрытия*. 2022;(3):4–23.
  19. Sanin V.V., Aheiev M.I., Kaplanskii Yu.Yu., Loginov P.A., Bychkova M.Ya., Levashov E.A. The effect of dopants on structure formation and properties of cast SHS alloys based on nickel monoaluminide. *Materials*. 2023;16(9):3299. <https://doi.org/10.3390/ma16093299>
  20. Logunov A.V. Heat-resistant nickel alloys for gas turbine blades and discs. Moscow: Gazoturbinnye Tekhnologii, 2017. 854 p. (In Russ.)  
Логунов А.В. Жаропрочные никелевые сплавы для лопаток и дисков газовых турбин. М.: Газотурбинные технологии, 2017. 854 с.
  21. Zhang W.L., Li S.M., Fu L.B., Li W., Sun J., Wang T.G., Jiang S.M., Gong J., Sun C. Preparation and cyclic oxidation resistance of Hf-doped NiAl coating. *Corrosion Science*. 2022;195:110014. <https://doi.org/10.1016/j.corsci.2021.110014>
  22. Dingding Zhu, Xinli Wang, Peng Jia, Canying Cai, Jianyu Huang, Guangwen Zhou. One-dimensional  $\gamma$ -Al<sub>2</sub>O<sub>3</sub> growth from the oxidation of NiAl. *Corrosion Science*. 2023;216:111069. <https://doi.org/10.1016/j.corsci.2023.111069>

## Information about the authors

**Vitaly V. Sanin** – Cand. Sci. (Eng.), Leading Researcher of the Laboratory of Metallurgical Processes of JSC “Giredmet”; Researcher of the Scientific-Educational Center of SHS of MISIS–ISMAN.

<https://orcid.org/0000-0002-9983-654X>

E-mail: vivsanin@rosatom.ru

**Maksym I. Aheiev** – Cand. Sci. (Eng.), Junior Researcher, Scientific-Educational Center of SHS of MISIS–ISMAN.

<https://orcid.org/0000-0003-2079-8710>

E-mail: aheievmi@gmail.com

**Pavel A. Loginov** – Cand. Sci. (Eng.), Researcher, Scientific-Educational Center of SHS of MISIS–ISMAN.

<https://orcid.org/0000-0003-2505-2918>

E-mail: pavel.loginov.misis@list.ru

**Marina Ya. Bychkova** – Cand. Sci. (Eng.), Assistant Prof. of National University of Science and Technology “MISIS” (NUST MISIS), Researcher of Scientific-Educational Center of SHS of MISIS–ISMAN.

<https://orcid.org/0000-0002-9233-4707>

E-mail: bychkova@shs.misis.ru

**Elizaveta S. Shukman** – Head of the Analytical Certification Center of JSC “Giredmet”.

<https://orcid.org/0000-0001-9999-6888>

E-mail: ESKoshel@rosatom.ru

**Liliya Yu. Mezhevaia** – Senior Researcher of the Analytical Certification Center of JSC “Giredmet”; Postgraduate Student of the Department of Certification and Analytical Control, NUST MISIS.

<https://orcid.org/0000-0001-9481-3149>

E-mail: lymezhevaya@rosatom.ru

**Vladimir N. Sanin** – Dr. Sci. (Eng.), Chief Researcher, Merzhanov Institute of Structural Macrokinetics and Materials Science of the Russian Academy of Sciences.

<https://orcid.org/0000-0001-8402-4605>

E-mail: svn@ism.ac.ru

**Tamara A. Lobova** – Dr. Sci. (Eng.), Prof. of the Department of Powder Metallurgy and Functional Coating of NUST MISIS.

<https://orcid.org/0009-0002-1749-0782>

E-mail: smazka39@mail.ru

## Информация об авторах

**Виталий Владимирович Санин** – к.т.н., вед. науч. сотрудник лаборатории металлургических процессов АО «Гиредмет», науч. сотрудник Научно-учебного центра (НУЦ) СВС МИСИС–ИСМАН.

<https://orcid.org/0000-0002-9983-654X>

E-mail: sanin@misis.ru

**Максим Игоревич Агеев** – к.т.н., мл. науч. сотрудник НУЦ СВС МИСИС–ИСМАН.

<https://orcid.org/0000-0003-2079-8710>

E-mail: aheievmi@gmail.com

**Павел Александрович Логинов** – к.т.н., науч. сотрудник НУЦ СВС МИСИС–ИСМАН.

<https://orcid.org/0000-0003-2505-2918>

E-mail: pavel.loginov.misis@list.ru

**Марина Яковлевна Бычкова** – к.т.н., доцент Национального исследовательского технологического университета «МИСИС» (НИТУ МИСИС), науч. сотрудник НУЦ СВС МИСИС–ИСМАН.

<https://orcid.org/0000-0002-9233-4707>

E-mail: bychkova@shs.misis.ru

**Елизавета Сергеевна Шукман** – начальник испытательного аналитико-сертификационного центра АО «Гиредмет».

<https://orcid.org/0000-0001-9999-6888>

E-mail: ESKoshel@rosatom.ru

**Лилия Юрьевна Межевая** – ст. науч. сотрудник испытательного аналитико-сертификационного центра АО «Гиредмет», аспирант кафедры сертификации и аналитического контроля НИТУ МИСИС.

<https://orcid.org/0000-0001-9481-3149>

E-mail: lymezhevaya@rosatom.ru

**Владимир Николаевич Санин** – д.т.н., гл. науч. сотрудник Института структурной макрокинетики и проблем материаловедения им. А.Г. Мерджанова РАН (ИСМАН).

<https://orcid.org/0000-0001-8402-4605>

E-mail: svn@ism.ac.ru

**Тамара Александровна Лобова** – д.т.н., профессор кафедры порошковой металлургии и функциональных покрытий НИТУ МИСИС.

<https://orcid.org/0009-0002-1749-0782>

E-mail: smazka39@mail.ru

## Contribution of the authors

**V.V. Sanin** – determined the research's objective and conceptual framework, wrote the article, executed the synthesis processes, performed additional metallurgical processing, and engaged in the discussion and documentation of the findings.

**M.I. Aheiev** – defined the work's aim and conceptualization, contributed to writing the manuscript, conducted microstructural examinations, X-ray diffraction structural analyses, mechanical testing, and assessments of heat resistance, participated in discussions and the elucidation the results.

## Вклад авторов

**В.В. Санин** – определение цели работы и концепции исследований, написание статьи, проведение синтезов, проведение дополнительных металлургических процессов, обсуждение и описание результатов.

**М.И. Агеев** – определение цели работы и концепции исследований, написание статьи, проведение микроструктурных исследований, рентгенофазового структурного анализа, механических испытаний, испытаний на жаростойкость, обсуждение и описание результатов.

**P.A. Loginov** – focused on transmission microscopy investigations, contributed to the discussions, interpretation of the results, and co-authored the article.

**M.Ya. Bychkova** – participating in the discussion of the research concept and results, describing the results of the X-ray diffraction structural analysis and microstructural studies.

**E.S. Shukman** – undertook the analysis to ascertain the chemical composition of the alloys, described these findings, and participated in the deliberation of the results.

**L.Yu. Mezhevaia** – carried out the investigation of metallographic sections using optical microscopy, evaluated the non-metallic inclusions, documented the chemical composition results, and contributed to the discussion of the findings.

**V.N. Sanin** – engaged in conceptual discussions, undertook synthesis and metallurgical processing tasks, and participated in analyzing and discussing the research outcomes.

**T.A. Lobova** – defined the research direction and framework, took part in discussions on the findings, and described the outcomes of the mechanical tests.

**П.А. Логинов** – проведение исследований методом просвечивающей микроскопии, описание результатов и их обсуждение, написание статьи.

**М.Я. Бычкова** – участие в обсуждении концепции исследований, участие в обсуждении результатов, описание результатов рентгенофазового структурного анализа и микроструктурных исследований.

**Е.С. Шукман** – проведение исследований по определению химического состава, описание результатов и участие в их обсуждении.

**Л.Ю. Межевая** – исследование металлографических шлифов методом оптической микроскопии, проведение оценки неметаллических включений, описание результатов определения химического состава, участие в обсуждении результатов.

**В.Н. Санин** – участие в обсуждении концепции исследований, проведение синтезов и металлургических переделов, обсуждение результатов исследований.

**Т.А. Лобова** – определение цели работы и концепции исследований, обсуждение результатов исследований, описание результатов механических испытаний.

*The article was submitted 29.01.2024, revised 12.02.2024, accepted for publication 14.02.2024*

*Статья поступила в редакцию 29.01.2024, доработана 12.02.2024, подписана в печать 14.02.2024*